Ionizing vs collisional radiation damage in materials: separated, competing, and synergistic effects in Ti_3SiC_2

William A. Hanson[a,*], Maulik K. Patel[a,b], Miguel L. Crespillo[a], Fuxiang Zhang[c], Steven J. Zinkle[a,c], Yanwen Zhang[a,c], William J. Weber[a,c,*]

[a]*Department of Materials Science & Engineering, The University of Tennessee, Knoxville, TN, 37996, USA*
[b]*Department of Mechanical, Materials & Areospace Engineering, University of Liverpool, L69 3GH, UK*
[c]*Materials Science & Technology Division, Oak Ridge National Laboratory, Oak Ridge, TN, 37831, USA*

* Corresponding authors:
(W.A. Hanson) *email:* whanson@vols.utk.edu;
(W.J. Weber) *email:* wjweber@utk.edu;

Abstract

Comparison between intense radiation environments present in nuclear reactors and charged particle beams is necessary for evaluating next generation fission and fusion reactor materials. However, these two irradiation environments encompass different proportions of ionizing and collisional phenomena, so exploring the different energy loss pathways is needed for appropriate analysis. Using the candidate $M_{n+1}AX_n$ phase, Ti_3SiC_2, as a test case, this work separates the effects of electronic and nuclear energy loss during ion irradiation, through a combination of 4 *MeV* Au, 17 *MeV* Pt, and 14 *MeV* Cl ion irradiations to examine the effects independently and systematically recombine them. Nuclear energy loss (elastic collisions) is found to be primarily responsible for the formation of a face-centered-cubic phase with anti-site defects, while intense electronic energy loss (ionization) exacerbates the effect and increases lattice strain. Further, these dissipation pathways are found to be competing or synergistic depending on their ionization and collisional ratio.

Keywords: Ion irradiation damage; Ti_3SiC_2 MAX Phase; X-ray diffraction (XRD); Transmission electron microscopy (TEM); Electronic and nuclear energy loss synergy

1. Introduction

Irradiation with charged particles (ions) is a powerful tool, in use for decades, for understanding the damage evolution of materials exposed to radiation environments. It is well established that elastic collisions with atomic nuclei or nuclear energy loss (S_n) during ion irradiations will produce elastic collision cascades and defects similar to those observed following neutron irradiation [1-6]. There are additional benefits of a greater control over the irradiation environment, reduced irradiation time, and little to no resultant radioactivity following ion irradiation. This is with the recognition that higher energy ions have a significant increase in inelastic collisions with electrons, electronic energy loss (S_e). These electronic interactions dominate the energy transfer until the energy, and thus velocity, of the ion is reduced sufficiently for the elastic scattering cross section to increase and nuclear energy loss to dominate the interactions [1-6]. It is well established that there is variation in material response between these two energy loss pathways [3,4,7,8]. However, early observations and current studies show that ionizing radiation can enhance the diffusion of defects and impurities and even result in annealing of displacive damage in both metallic and ceramic systems from nuclear energy loss during low-energy, heavy ion irradiation [3,4,7,8]. More recent studies have demonstrated that, depending on the material system and initial defect concentrations, increasing the ratio of S_e/S_n can enhance the damage production along the ion path [9] or suppress damage production through in-cascade annealing [8,10]. The importance of this variation in S_e/S_n applies to direct comparison with reactor irradiation environments as well due to intense ionization from gamma radiation and electronic energy loss of primary recoils produced by collisions with neutrons. This ratio of overall S_e/S_n will vary depending on the gamma and neutron energy spectra and material. For example, a ratio of around 4 is typical for liquid metal cooled fast fission reactors while a mixed spectrum light water reactor (LWR) has a S_e/S_n ratio greater than 100 [11].

This all accentuates that knowing the response of materials to intense ionization is vital to effectively utilizing ions as a complimentary tool to studying neutron irradiation environments. Of particular interest is the irradiation response of $M_{n+1}AX_n$ (MAX) phases, which are a class of ternary carbides and nitrides under consideration as a structural material for future generation fission and fusion reactors. These crystallize in a hexagonal, nanolamellar structure with basal planes of A group elements separating n M_2X rhombohedra, where M is an early transition metal and X is either C or N, see supplementary figure (S.Fig. 1a). This layered polycrystalline structure leads to a unique combination of properties for ceramics, including high thermomechanical phase stability, high thermal conductivity, corrosion resistance, and low neutron absorption cross section for several compositions [12-18], all of which make them an attractive candidate for cladding and core material applications [19,20]. This has led to numerous neutron and ion irradiation studies, especially for the widely available Ti-based MAX phases (Ti_3SiC_2, Ti_3AlC_2, and Ti_2AlC) [21-31], Ti_3SiC_2 being the focus of this study. Because of the nanolamellar structure, Ti_3SiC_2 has a very high interfacial density and thus a very high theoretical sink strength for point defects and a high diffusivity path for recombination [20,28,30,32], which seems to result in a resistance to some forms of irradiation damage [27,28,33,34]. However, this MAX phase does exhibit irradiation damage, namely an increase in the c/a ratio of the c and a lattice parameters (c and a-LPs, respectively) and an increase in signal attributed to TiC_x, the current understanding of which must be explained [23,25,27,29-31,33,35].

TiC_x, henceforth referred to as TiC for simplicity, may form during synthesis of Ti-based MAX phases as a stoichiometric mismatch impurity as it shares much of the MAX structure, specifically, Ti_3SiC_2 lacking its A-layer is a nanotwinned $TiC_{0.67}$ structure. TiC has a lower thermal conductivity and is more brittle than Ti_3SiC_2, so its formation will serve to partially offset the attractive properties of the MAX [14,15,17,27]. The precise mechanism by which

TiC concentration would increase in the MAX is not agreed upon, mainly due to difficulty in exactly quantifying the increases given the similarity of the structures. Some suggest that a phase decomposition from the MAX phase to the stoichiometrically C-deficient TiC_x occurs [24,25,27,36]. However, a recent study by Wang *et al.* has demonstrated that following low-energy Au irradiations, the Ti_3AlC_2 composition, which shares its structure with Ti_3SiC_2, does not decompose, retains its stoichiometry, and actually forms a twinned face-centered-cubic (FCC) MAX structure, following the twinned TiC structure through anti-site formation between the M and A-elements [37,38]. That said, regardless of the mechanism, the increase in the FCC-type phase typically attributed to TiC in x-ray diffraction (XRD) profiles is still a relatively well-established qualitative metric for irradiation damage in Ti_3SiC_2 [22,24,31,39].

Though Ti_3SiC_2, and MAX phases in general were previously thought insensitive to electronic excitations and ionization effects [23], a recent study using 9 *MeV* Ti ions discovered that above a threshold electronic energy loss of 4 $keV\ nm^{-1}$, increases in c/a and a signal attributed to TiC were observed [31]. This effect was found to be independent of damage dose (dpa) and demonstrated the importance of electronic energy loss in the material response to ion irradiation. However, as Ti is a medium mass ion with little variation in S_n over the depths investigated, the effects of the elastic and inelastic collisions must be separated to fully understand the response.

As indicated earlier, previous studies in other material systems have used a combination of irradiations to explore independent separate effects of S_e and S_n, typically by introducing initial defects into the material (pre-damaging) through low-energy, heavy ion irradiations, where S_n is dominant, and comparing with high-energy ion irradiations, where S_e is dominant. The subsequent recombination of these different energy loss pathways through sequentially performing these irradiations often reveals a synergy or competition between them, whereby the evolving defect concentration affects the energy dissipation of inelastic collisions and vice

versa [4,7,9,10,40-42]. By comparing high-energy Pt and Cl ion irradiation of pristine and pre-damaged Ti_3SiC_2, as well as pristine Ti_3SiC_2 irradiated with high-energy Ti ions as an intermediate S_e/S_n case, this work seeks to use similar methods to further deconvolute electronic and nuclear energy loss effects and explore their potential additive, synergistic, and or competing nature.

2. Experimental

2.1. Physical Sample Preparations

Polycrystalline Ti_3SiC_2 was obtained as synthesized in bulk by the Drexel University Layered Solids group. Complete details for the hot-pressing method have been discussed in depth previously, so they will not be repeated here [3,43]. A low speed, counter-balanced diamond saw was used to section plate samples, which were subsequently polished with diamond lapping film grits and finished with 0.05 μm alumina slurry. Plates were ultrasonically washed with deionized water and 99.9% pure ethanol to remove alumina and polishing remnants. Final irradiation dimensions of 6×4.5 *mm* were cut using the same diamond saw, and samples were washed using the same method. Transmission electron microscopy (TEM) lamella were prepared in cross section from the irradiation surface using a Zeiss Auriga Crossbeam scanning electron microscope equipped with a Ga focused ion beam (FIB) located at the Joint Institute for Advanced Materials (JIAM) microscopy facility. The irradiation surface was protected with a Pt deposition layer and low FIB milling currents were used during polishing to minimize any polishing surface amorphization artifacts.

2.2. Ion Irradiations

Full cascade SRIM (v2013) [44,45,46] simulations were conducted utilizing weighted average threshold displacement energies of 25.7, 30.6, and 27.9 *eV* for Ti, Si, and C, respectively, as determined by previous *Ab initio* molecular dynamics simulations by Liu *et al.* [47]. As pristine lattice parameters closely match those in the literature, a theoretical density of 4.528 $g\ cm^{-3}$ was selected for the simulations [17].

For the nuclear energy loss dominated irradiation, 4 *MeV* Au^{2+} was selected, see Fig. 1a, because it has sufficient energy to introduce damage to a depth of approximately 0.75 μm in the sample. This can be easily seen by examining the collision cascades, plotted using pysrim [46], for 5000 of the simulation ions as a function of depth in Fig. 1d and radially over the highlighted depths of 0.5 μm−0.75 μm in Fig. 1g. At the same time, the S_e does not exceed the ionization threshold established in the previous study of 4 $keV\ nm^{-1}$ [31]. A fluence of 5×10^{14} cm^{-2} was selected, which results in a peak damage dose of 3 dpa at ~0.5 μm. It was also established in the previous study that a change in ion concentration of 1000 *appm* resulted in no recorded change in strain in the material [31]; therefore, the ion concentration peak from this irradiation of < 250 *appm* with inert Au ions should result in no physical or chemical artifacts.

Two ions were selected for the electronic energy loss dominated irradiations: 17 *MeV* Pt^{5+} and 14 *MeV* Cl^{4+}. Each of these ions has a nearly identical and consistent S_e profile as a function of depth, see Fig. 1b and 1c, each of which exceeds the aforementioned 4 $keV\ nm^{-1}$ threshold over the depths of interest for this study, (0.5 μm − 0.75 μm). However, due to the large difference in mass, and associated nuclear scattering cross sections, they each have a vastly different ratio of electronic to nuclear energy loss (S_e/S_n). This may be easily visualized with the collision cascades, both as a function of depth and radially, as shown in Fig. 1e, 1f, 1h, and 1i. The same fluence of 1.76×10^{15} cm^{-2} was selected for both the 17 *MeV* Pt and 14 *MeV* Cl irradiations to result both a similar S_e dose and a damage dose for the Pt ions that matches the pre-damage dose of 3 dpa, see Fig. 1b. The lower S_n for Cl will result in a significantly lower damage dose, see Fig. 1c. In addition, pristine Ti_3SiC_2 was irradiated with 9 *MeV* Ti ions to reproduce the 2.8×10^{16} cm^{-2} fluence from the previous study in this batch of material. This not only allows for direct comparison between the studies, but the shallower irradiation depths provide an intermediate S_e/S_n with similar S_e to those of the high-energy Pt

and Cl ions [31]. A complete list of these irradiation conditions is provided for reference in supplemental table 1.

All ion irradiations were conducted at The University of Tennessee Ion Beam Materials Laboratory (IBML) [48]. Irradiations were conducted at room temperature with samples oriented normal to the beam. For each irradiation condition, the beam was defocused and wobbled slightly, and beam current was monitored closely to both track the dose and keep the flux below $4.5\times10^{11}\ cm^{-2}s^{-1}$ to minimize beam heating and charge accumulation [49].

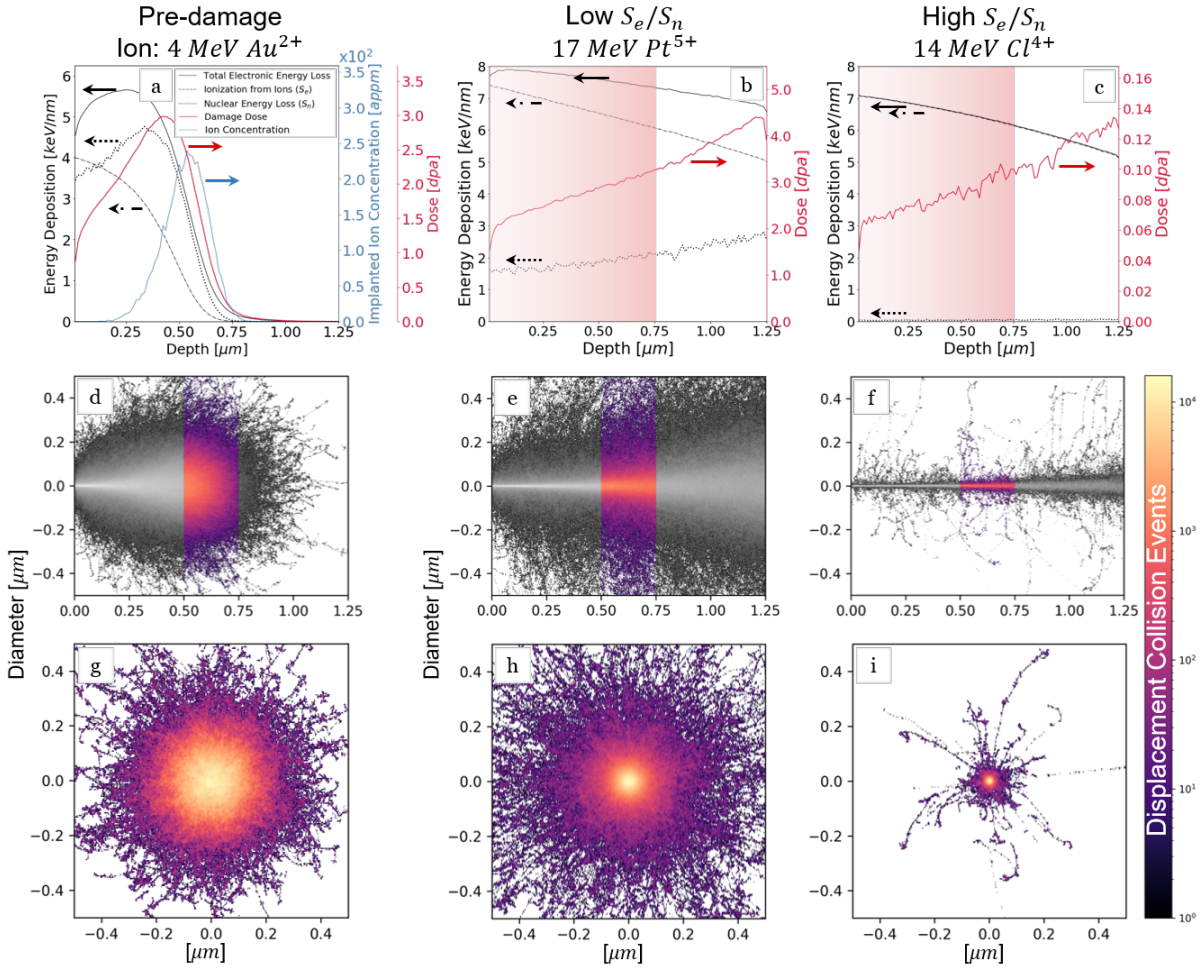

Fig. 1 – (a-c) Energy deposition and damage dose (dpa) as a function of depth for 4 *MeV* Au at a fluence of $5\times10^{14}\ cm^{-2}$ and 17 *MeV* Pt and 14 *MeV* Cl each at a fluence of $1.76\times10^{15}\ cm^{-2}$. It should be noted that the small S_n component for 14 *MeV* Cl results in a near overlap of the S_e and total electronic energy loss curves in (c). The shaded gradient in the backgrounds of (b) and (c) indicates the depth region influenced by 4 *MeV* Au ions in pre-damaged conditions, as detailed in (a). (d-f) collision cascade events for 5000 ions vs. depth for each ion,

respectively. (g-i) radial collision cascade events over the depth range of 0.5 μm to 0.75 μm as indicated by the colored bands in (d-f), respectively [49].

2.3. Characterization

Grazing incidence x-ray diffraction (GIXRD) profiles were gathered at the JIAM Diffraction Facility using a PANalytical X'Pert^3 MRD in grazing geometry equipped with a Cu x-ray tube, Si parabolic mirror, 0.04 *Rad* soller slits, 1/8° divergence slit, and a 0.27° parallel plate collimator. As in the previous study [31], penetration depth is defined as the depth normal to the surface, where the x-ray attenuation length ($I/I_0=1/e$) is reached. This is determined by the incident grazing angles, 2.25° and 3.25°, which result in penetration depths of ~0.5 μm and ~0.75 μm, respectively.

Initial and post irradiation TiC content was estimated to appropriately select the grazing angles, as TiC is a slightly better x-ray attenuator than Ti_3SiC_2, making use of the X-ray Interactions with Matter data tables developed by The Center for X-ray Optics [50]. That said, it is conventional to use consistent grazing angles between compared samples, even though variation in FCC-type profiles, whether a TiC phase or FCC-MAX, is expected following ion irradiation given previous results in the literature [22,24,31,39]. Therefore, an upper bound of 20% error is assumed in the TiC concentration estimations, which, due to the similarity between Ti_3SiC_2 and TiC x-ray attenuation, results in an average maximum calculated depth error of 0.04 μm. Therefore, the grazing angles of 2.25° and 3.25°, result in penetration depths of 0.5±0.04 μm and 0.75±0.04 μm, respectively, in each sample.

Scans were gathered over a range of 7-82° 2θ with a 0.02° 2θ step size and a count time of 3 *s*/*step*. Longer 9 *s*/*step* scans over the sub-ranges of 32-47° 2θ, 57-65° 2θ, and 70-81° 2θ were gathered using the same step size for better counting statistics in regions were peak shifting was expected. All pristine conditions prepared above were compared in the pre-irradiation state using two grazing depths and a count time of 3.5 *s/step*, and all peak positions were found to be statistically consistent.

To perform strain analysis using GIXRD, each profile was corrected to appropriately account for the absorption associated with the grazing geometry, the peaks were individually fitted using a Voigt or Gaussian function as needed in OriginPro (v2018) [51], and a stable iterative method was utilized to determine a self-consistent c/a [31,52]. This method provides precise estimation of the c and a-LPs and subsequent strain while using a lab-scale diffractometer. As a reiteration of the description from the previous study, since each fit peak contributes to determining the c/a for the profile, each peak must also contribute to the resulting lattice parameters; therefore, any plotted c and a-LPs resulting from this method are the averages of each fit peak with the standard deviation plotted as error bars. The exact implementation of this method has been fully detailed previously [31,35,52].

Raman spectroscopy was used to corroborate some observations in grazing diffraction profiles using a Horiba LabRaman HR evolution with 785 *nm* laser, 600 *gr*/*mm* grating, 5×20 *s* count times, and a 100× objective. The scans were conducted over the wavenumber range of 70−1800 cm^{-1}.

TEM was performed using a Zeiss Libra 200 HT FE MC in the JIAM microscopy facility. Selected area electron diffraction (SAED) patterns, with an illuminated region diameter of ~250 *nm*, were gathered in ~100 *nm* increments from the sample surface to produce a SAED depth profile of the irradiation cross section.

3. Results

3.1. Grazing Incidence X-ray Diffraction

The 9 *s/step* reduced range GIXRD profiles for each of the five damage states are plotted in Fig. 2, along with the 3.5 *s/step* pristine profile. The profiles had their backgrounds stripped, were normalized, and vertical dashed lines mark the major peak centers of the pristine profile. The relative intensity is plotted in the background as a heat map to more clearly display changes in peak position and intensity between the vertically staggered profiles. The vertical staggering is also in order of increasing S_e/S_n with Au ion pre-damaged

material plotted higher than samples only exposed to high S_e ions. A depth of 0.5 μm was probed for the 9 *MeV* Ti irradiated sample as this corresponds to a S_e of ~5.1 $keV\ nm^{-1}$ and a damage dose of ~4 dpa, similar to those achieved with the Pt and Cl irradiations.

It may be observed immediately that broad FCC-type peaks, previously attributed to TiC [31] and marked with boxes, are present in each sample pre-damaged with 4 *MeV* Au ions, and are highly dominant in samples irradiated with 17 *MeV* Pt ions. As detailed by full cascade SRIM (v2013) [44,45,46] simulations, plotted in Fig. 1b and 1c, each of these conditions has a significant S_n contribution. On the other hand, material irradiated with the lower S_n of 14 *MeV* Cl ions shows little to no intensity from these broad peaks, further evidenced by the sharp, albeit shifted, intensity of the principle MAX peaks in the heat map. There is a lack of any diffuse intensity of the FCC-type signatures in the relative intensity heat map despite having a comparable S_e to the high-energy Pt ions, see Fig. 1b and 1c. It should be noted that the S_e/S_n at the depths probed for the Pt and Cl ions may be comparable to that of a fast fission and mixed spectrum LWR, respectively [11]. This variation in S_e/S_n with similar S_e may be observed as peak shifting in Fig. 2. Peaks closely aligned with the c and a axis shift to lower and higher *degrees 2θ*, respectively. This is evident when observing peaks such as the (104), (008), and (105) in Fig. 2a, the (109) in Fig. 2b, and the (1012) and (118) in Fig. 2c, each of which shifts to a lower *degrees 2θ*, indicating a relative expansion of the c-LP. Meanwhile, the principle peak parallel with the a-axis, the (110) can be seen to shift to higher *degrees 2θ* in Fig. 2b, which corresponds to a slight contraction of the a-LP. The shifting of c-LP dominated peaks may also be readily observed in the full profiles plotted in S.Fig. 2. It is interesting to note that this shifting appears isolated from dose given that the greatest peak shifts are observed following the Cl ion irradiations, which induced the lowest damage dose, but had the highest S_e/S_n per ion.

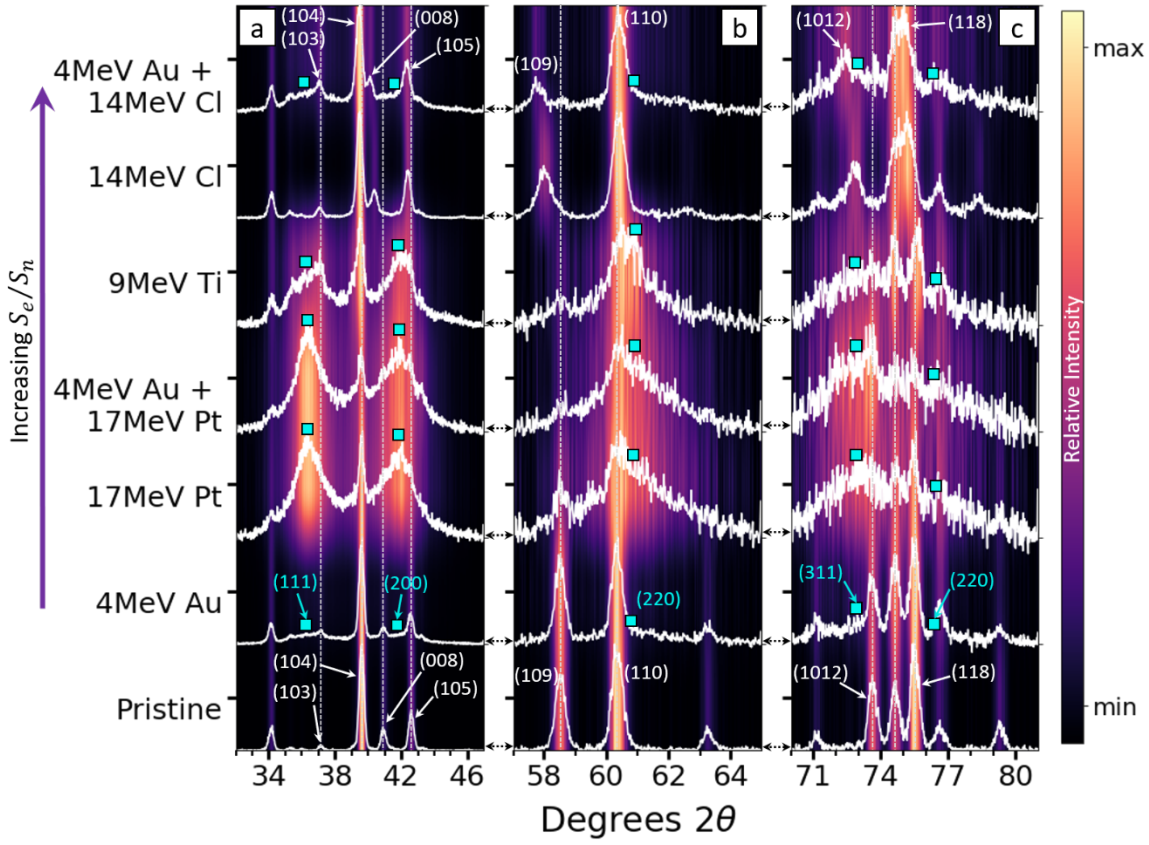

Fig. 2 – GIXRD profiles of the subranges (a) 32-47° *2θ*, (b) 57-65° *2θ*, and (c) 70-81° *2θ* at a depth of 0.75 *μm* comparing pristine and irradiated conditions, including a repetition of the lowest fluence (2.8×10^{16} cm^{-2}) 9 *MeV* Ti irradiation from the previous study at a depth of 0.5 *μm*, which represents a similar S_e and damage dose [31]. All irradiated profiles were gathered at the 9 *s/step* extended count times, and the pristine profile was gathered at 3.5 *s/step*. Profiles are staggered vertically with increasing S_e/S_n, and relative intensity plotted in the background as a heat map, along with dashed vertical reference lines marking the centers of major pristine peaks, assist in discerning changes in peak intensity and position between the staggered profiles.

The broad FCC-type peaks observed in these diffraction profiles have been previously observed following high fluence 4 *MeV* Au, 2 *MeV* I, 700 *keV* C, and 9 *MeV* Ti ion irradiations. They were attributed to TiC based on their position in reciprocal space and the presence of a small amount of initial impurity in the pristine material [23,24,25,31,36]. However, in light of the recent results in Ti_3AlC_2, which shares its structure with the subject of this study, a FCC-MAX phase transition should be considered as a mechanism behind the FCC type profiles observed in Fig. 2 [37,38]. Ti-Si anti-site defects are likely following

ballistic mixing via elastic collision cascades, as both Ti and Si are relatively easy to displace [47] and the proposed defect is known to have a favorably low formation energy [30,32,53]. It is further proposed that irradiation assisted diffusion, along with ballistic mixing may result in a site shift for the previous Si A-layer to the β-Ti_3SiC_2 position, see S.Fig. 1b, thus also creating interstitial sites for C_{int} identical to the typical C site position. This may result in the twinned FCC structure shown in S.Fig. 1c and 1d, which retains the Ti_3SiC_2 stoichiometry, but effectively lacks the A-layer, as the Ti-Si anti-sites are more akin to a solid solution.

From a diffraction standpoint this proposed mechanism seems plausible. It is important to recognize the similarity of diffraction planes of this defined hexagonal structure to the twinned FCC structure embedded inside it. The hexagonal {103}, {105}, {110}, {1012}, and {205} peaks are emphasized by the Ti-Si anti-sites and also intersect the FCC-MAX {111}, {200}, {220}, {311}, and {222}, see S.Fig. 1e to 1i. Further, slight distorting of the hexagonal lattice results in a complete overlap with these FCC positions, as observed experimentally. Of note is the presence of these broad FCC-MAX profiles only following irradiation with 17 *MeV* Pt ions, 9 *MeV* Ti ions, and 4 *MeV* Au ions. These broad peaks are markedly absent when pristine material is irradiated with 14 *MeV* Cl ions; though, their intensity may increase slightly when pre-damaged material is irradiated by the same conditions. This seems to suggest that only ions with a larger S_n component will lead to this FCC-MAX formation, which is consistent with elastic collision cascades, see Fig. 1d to 1i, resulting in the necessary Ti-Si anti-site formation. This observation is consistent with profiles gathered in the literature that exhibit these broad FCC-type profiles and also contain a larger S_n component [23,24,25,31,36].

3.2. Raman Spectroscopy

The pristine and irradiated Raman spectra are plotted in Fig. 3. There are Raman active modes present in the pristine Ti_3SiC_2 spectra at 159, 190, 222, 275, 370, 620, and 676 cm^{-1}.

Following Au pre-damaging irradiations and high-energy Pt irradiations, the modes centered at 190, 275, and 676 cm^{-1} lose their intensities, and the mode at 370 cm^{-1}, which is attributed to both Ti_3SiC_2 and $TiC_{0.67}$, is sharpened slightly. Additional modes attributed to $TiC_{0.67}$ appear at about 250 and 340 cm^{-1}, and a broad mode appears at about 596 cm^{-1}. The already broad modes centered at 222 and 370 cm^{-1} remained following each irradiation state; however, the mode at 159 cm^{-1} is broadened following Au pre-damaging and high-energy Cl irradiations, and may be lost following high-energy Pt irradiations. Unlike the heavy ion irradiations, the very intense modes at 275, 620, and 676 cm^{-1} remain following high-energy Cl irradiations, though they lose intensity, broaden, and shift to slightly lower frequencies. Note that in this case, the 9 *MeV* Ti ion irradiation is not included in this comparison because its energy dissipation varies significantly with depth, while the energy dissipation with depth is mainly flat for the separate effects study conditions.

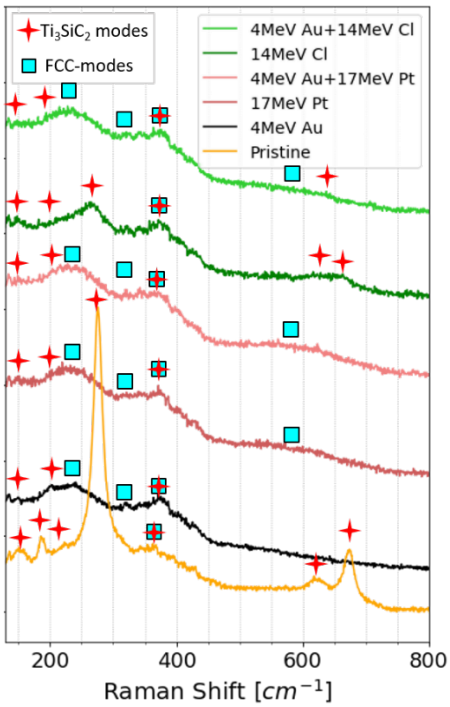

Fig. 3 – Raman shift over the wavenumber range of 70-800 cm^{-1} comparing pristine and ion irradiated conditions with increasing S_e/S_n.

Examination of the Raman spectra in Fig. 3 appears to corroborate the above proposal of both the FCC-MAX phase formation and its link to a larger S_n component. All $TiC_{0.67}$ defect modes are present in the Ti_3SiC_2 spectra; though, they are shifted and the order of the C-sites makes them far more intense and sharp [54]. Since, the FCC-MAX shares its Ti:C ratio and structure with $TiC_{0.67}$, most notably its effective lack of the basal A-layers, it is proposed that the following established $TiC_{0.67}$ modes should apply to the FCC-MAX structure as well. Spectra from samples exposed to a greater S_n, whether from pre-damaging with low-energy Au or exposed to high-energy Pt, show decrease in intensity from MAX related modes and increase in their $TiC_{0.67}$ counterparts.

The profiles with a large S_n contribution lose most intensity from the Ti_3SiC_2 A_{1g} modes, c-axis movement of C-Ti-C, at 275, 312 (likely hidden beneath the noise) and 676 cm^{-1} while gaining broad intensity from their $TiC_{0.67}$ counterparts at 340, 372 and 661 cm^{-1} (also likely buried in the background). The E_{1g} mode, a-axis movement of C-Ti-C in symmetry about the basal A-layers, is also lost in these cases and replaced by broad intensity near its counterpart at 596 cm^{-1} [17]. The formation of C Frenkel pairs and interstitials as described in the above FCC-MAX phase structure could explain this as the C occupancy in the Ti-octahedra approaches that seen in $TiC_{0.67}$, thus resulting in the broader, shifted modes [54]. Further, the E_{2g} mode, a-axis movement of C-Ti-Si, mode at 222 cm^{-1} broadens and is joined by its $TiC_{0.67}$ shifted counterpart at about 250 cm^{-1} [17]. Once again, the spectra for the condition with Cl ion irradiation, where S_n is significantly lower, does not include these additional $TiC_{0.67}$ modes, save a slightly sharper mode at 370 cm^{-1}, which again is shared between Ti_3SiC_2 and $TiC_{0.67}$. This condition further retains the A_{1g} and E_{1g} modes albeit broadened by local defects and slightly shifted from 275, 620, and 676 cm^{-1}. It should be noted that while the $TiC_{0.67}$ modes are present, the MAX phase does not appear to be eliminated. The E_{2g} modes located at 159 cm^{-1}, unique to Ti_3SiC_2, and 222 cm^{-1}, each require the basal A-layer and retain much

of their intensity following each irradiation condition, only broadening slightly [54,55]. These results further suggest that nuclear energy loss is principally responsible for the formation of the FCC-type phase embedded in the MAX structure.

3.3. Lattice Parameter Analysis

The iterative method detailed previously [31] was used to determine a self-consistent c/a over each depth range probed in irradiated and pristine samples, and subsequent c and a-LPs were calculated. The $\Delta c/c_0$ and $\Delta a/a_0$, i.e. the out-of-plane and in-plane strain, respectively, for the different irradiation conditions are plotted as a function of S_e/S_n in Fig. 4 with a horizontal reference line for the pristine c and a-LPs and their standard deviations shown for reference. As in Fig. 2, the $\Delta c/c_0$ and $\Delta a/a_0$ from the previous Ti irradiation condition are plotted in Fig. 4 as well. Lattice strains have also been calculated and included in Fig. 4 for c and a-LPs reported in the literature following room temperature 7 *MeV* Xe irradiations [39] and room temperature 92 *MeV* Xe and 74 *MeV* Kr irradiations [23,56]. These irradiations are to damage doses that are similar to the other irradiation conditions in their respective S_e/S_n regimes [23,39,56]. However, it should be noted that following the low-energy Xe irradiation, error was not reported in the literature for the lattice parameter determination [39], so error was conservatively estimated at 0.1% of the reported lattice strain in this case and included as error bars.

Comparing the lattice strain of each condition to S_e/S_n confirms the initial peak shifting observations in Fig. 2 and reveals a trend. As S_e/S_n increases, the c/a distortion appears to increase and eventually reach a maximum, with the c-LP expansion and a-LP contraction maximized by S_e/S_n of ~150 and ~250, respectively. Further, pre-damaged samples show a lattice strain from pristine values that is greater than the sum of the strains for both the low-energy Au ion irradiations and high-energy Pt or Cl ion irradiations; though, the trend of increasing c/a distortion remains correlated with an increase in S_e/S_n.

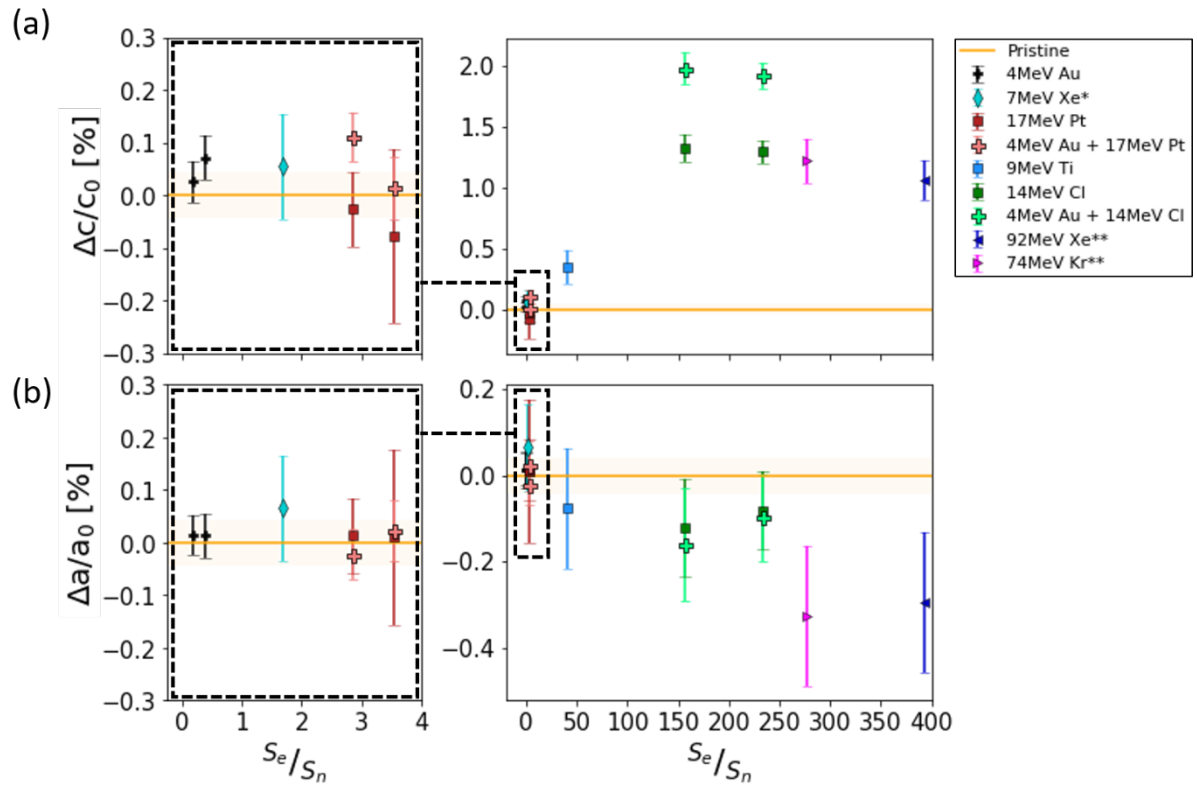

Fig. 4 – (a) and (b) c and a lattice strain ($\Delta c/c_0$ and $\Delta a/a_0$, respectively) as a function of the ratio of electronic to nuclear energy loss (S_e/S_n) with an expanded view of the low S_e/S_n range. Included are $\Delta c/c_0$ and $\Delta a/a_0$ values from this work as well as 7 *MeV* Xe* ion irradiations to 3 dpa [39], 92 *MeV* Xe** ion irradiations to 0.14 dpa, and 74 *MeV* Kr** ion irradiations to 0.09 dpa [23,56] from the literature.

In each case, the high-energy Cl irradiations resulted in a significant expansion of the c-LP and contraction of the a-LP while high-energy Pt resulted in much less lattice strain, and low-energy Au showed little change from pristine values. Recall that the 14 *MeV* Cl and 17 *MeV* Pt S_e vs. depth behavior is comparable, and each was irradiated to the same 1.76×10^{15} cm^{-2} fluence to ensure a similar S_e deposition, which exceeds the previously observed 4 $keV\ nm^{-1}$ threshold to lattice strain following Ti ion irradiations [31]. In this case, however, Cl has a significantly greater S_e/S_n than Pt, and the resulting strain increase is equally large, suggesting that when the 4 $keV\ nm^{-1}$ threshold in electronic energy loss is surpassed, the ratio between inelastic and elastic energy dissipation becomes more important. This is corroborated by the inclusion of the 9 *MeV* Ti irradiation, which has a similar S_e (~5.1 $keV\ nm^{-1}$) to the high-

energy Pt and Cl irradiations and damage dose (~4 dpa) to the Au and Pt irradiations. As shown in Fig. 4, the $\Delta c/c_0$ and $\Delta a/a_0$ for 9 *MeV* Ti falls directly on the trend established by the conditions in this study. The 92 *MeV* Xe and 74 *MeV* Kr irradiations are to damage doses of 0.14 and 0.09 dpa, respectively, and are comparable to the damage dose of 0.1 dpa reached by the 14 *MeV* Cl irradiations of this study. Their $\Delta c/c_0$ and $\Delta a/a_0$ values continue the trends of this study at greater S_e/S_n regimes, and like the Cl irradiations, their respective GIXRD profiles show no broad FCC-type peaks following irradiation [23,56]. Likewise, the lattice parameter values for the 7 *MeV* Xe irradiation were gathered from irradiation depths where the damage dose is 3 dpa, identical to the 4 *MeV* Au irradiations of this study. The material response also appears largely similar, with reduced lattice strain from pristine values and GIXRD profiles showing broad FCC-type peak signatures [39].

Inelastic energy dissipation can lead to the formation of point defects, which add to the strain observed. The ionization energy from the high-energy Cl and Pt ions, once transferred to the lattice via electron-phonon coupling, will result in a large thermal spike, expected to exceed 1000 *K* in the pristine Ti_3SiC_2, based on inelastic thermal spike calculations in SiC [57]. This large, rapid temperature differential has been demonstrated to result in a shock wave in the lattice, which can easily displace local atoms to the surrounding lattice [58], likely resulting in Frenkel pairs and Ti-Si anti-site formation. Since the typical sharpness in the pristine principle modes of the Raman spectra is due to the highly ordered C atoms, their slight broadening and shifting in the spectra of the 14 *MeV* Cl irradiated samples is evidence for their displacement to interstitial lattice sites. That said, based on the previous observations and the evidence for elastic collision events in Fig. 1c, it is unlikely the inelastic collisions are solely responsible for the defect production and resultant strain observed in Fig. 4, but rather serves to exacerbate the defect production of elastic scattering events, thus increasing the strain, the method of which will be discussed further below.

3.4. Transmission Electron Microscopy

A series of SAED depth profiles, oriented on the $[11\bar{2}0]$ zone axis are shown in Fig. 5 and 6 and S.Fig. 3 and may be used to further corroborate both the GIXRD and Raman spectroscopy results. Examining the profile of the nuclear energy loss dominated Au irradiations in Fig. 5b to 5d, the FCC-type twinned structure for the shared orientation, illustrated in Fig. 5g and 6g, is very clear, as simulated in Fig. 5f. Additionally, the Ti_3SiC_2 structure, α-polymorph simulated in Fig. 6f, is visible in Fig. 5b to 5d, gaining in relative intensity until it is the only phase present in Fig. 5e, which is beyond the 4 *MeV* Au ion range. Further, within the low-energy Au ion range, the periodicity present in the relative intensity of the MAX profile is more characteristic of the β-Ti_3SiC_2 polymorph, with the more uniform intensity of the α-polymorph returning by Fig. 5e. It should be noted at this point, that during the thinning preparation of the TEM lamella, the Au irradiation depth showed some signs of preferential thinning, even in regions intentionally left thick for tilting alignments, despite FIB milling parameters being matched to those utilized in other samples. That said, the results displayed here are not believed to be artifacts of the preparation process as these are typically exhibited as amorphous halos, observed previously in SAED patterns [31]. These SAED patterns by contrast, while highly disordered as indicated by the diffuse spots for the {111} twinned FCC-type structure, exhibit no such halos, and further, the Ti_3SiC_2 structure, visible at each depth from the irradiation surface, is highly ordered and crystalline with fine spots. In the literature, SAED patterns gathered following the 7 *MeV* Xe irradiations, included above in Fig. 4, also show a transition from the β-Ti_3SiC_2 periodicity in relative intensity to disordered FCC-twins [39].

Comparing the results for low-energy Au irradiation in Fig. 5 to those of the high-energy Ti irradiation in Fig. 6, it is possible to see the influences of electronic energy loss on the FCC-MAX formation. The FCC twins are not nearly as dominant in Fig. 6b to 6d, though

their diffuse intensity is still present at the appropriate positions in reciprocal space: FCC-type {111} and {002} in the vicinity of the MAX {103} and {105}, respectively. This is even observed across the grain boundary observed in Fig. 6a and 6b in a grain slightly misoriented from the defined $[11\bar{2}0]$ zone. Again, the periodicity more characteristic of the β-Ti_3SiC_2 polymorph is present and reduces in relative intensity until the α-Ti_3SiC_2 structure is again dominant by Fig. 6e, which is close to where S_e drops below the 4 $keV\ nm^{-1}$ threshold. This would seem to corroborate that when electronic energy loss exceeds the threshold, it exacerbates the predominantly elastic process of producing β-Ti_3SiC_2 with anti-site defects and then eventual FCC-MAX, as the nuclear energy loss for this ion at this irradiation depth is significantly lower than the Au ion in Fig. 5. If the MAX structure was decomposing into stoichiometrically deficient MX binary phase, the even transition from α-Ti_3SiC_2 to β-Ti_3SiC_2 to the {111} twinned FCC-type structure should not be present, along with the fine MAX pattern at each depth, as is observed in both Fig. 5 and 6. Therefore these results support both the GIXRD and Raman results and the mechanism proposed here to support the one recently proposed and demonstrated in the literature for the Ti_3AlC_2 composition [38].

As in the GIXRD results, the SAED depth profiles for high-energy Cl irradiations in S.Fig. 3 represent a contrast to those in Fig. 5 and 6 as they show no relative intensity from either FCC-type twins or the β-polymorph at any irradiation depth probed. α-Ti_3SiC_2 appears to be the dominant structure present at each depth, S.Fig 3b to 3d; though, there is significant diffuse streaking parallel to the $[0001]$ direction, which indicates a high density of defects and is expected given the large lattice strain observed in Fig. 4.

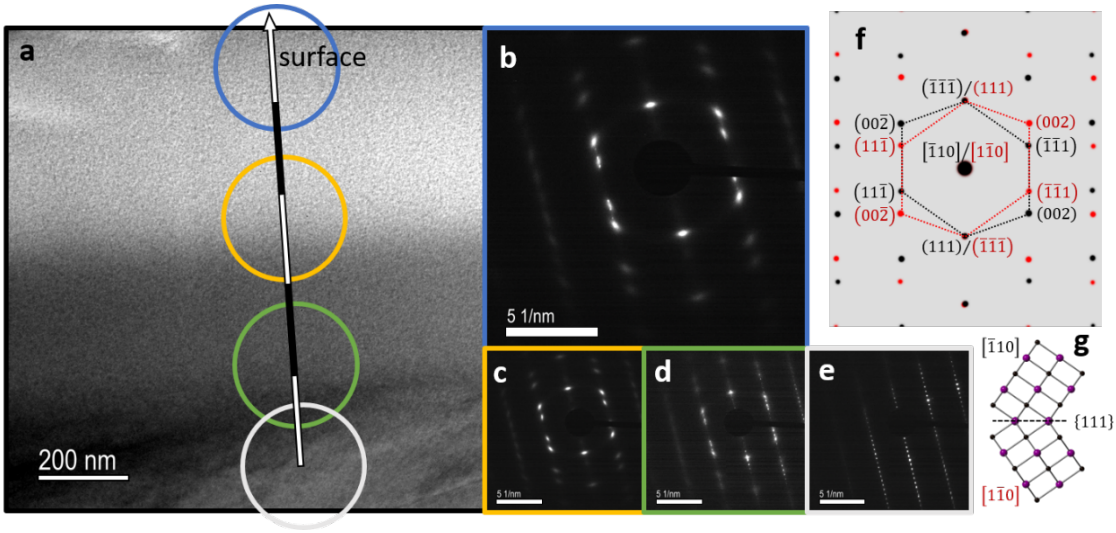

Fig. 5 – TEM SAED depth profile in the 4 *MeV* Au irradiated sample oriented on the $[11\bar{2}0]$ zone axis with (a) overview, (b-e) SAED patterns, (f) simulated diffraction pattern for the FCC-twin structure oriented on the $[\bar{1}10]/[1\bar{1}0]$ zone axes, which are equivalent in orientation to the MAX $[11\bar{2}0]$ or [110] zone, and (g) reference structural orientation.

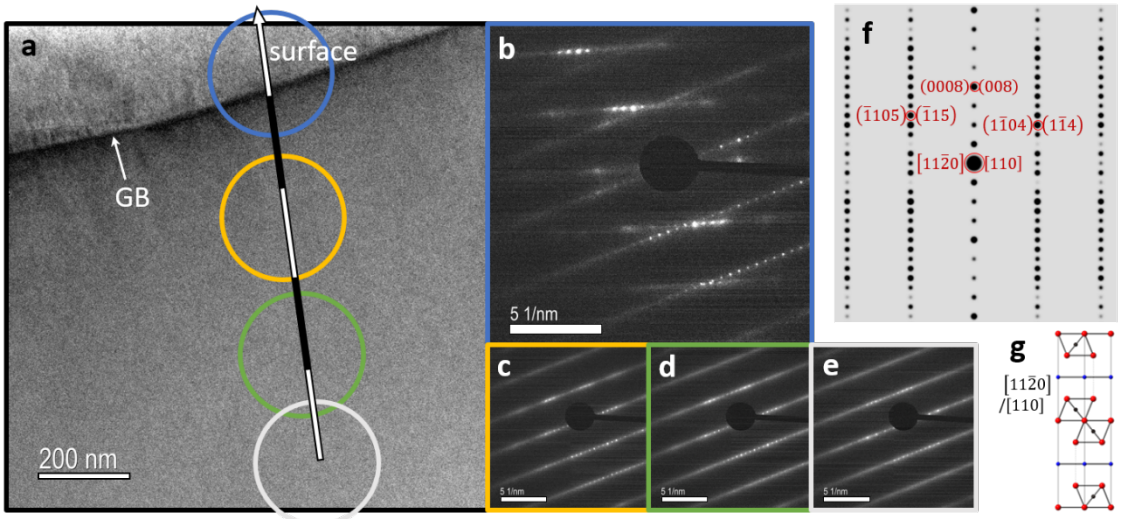

Fig. 6 – TEM SAED depth profile in the 9 *MeV* Ti irradiated sample oriented on the $[11\bar{2}0]$ zone axis with (a) overview, (b-e) SAED patterns, (f) simulated diffraction pattern for the Ti_3SiC_2 MAX oriented on the $[11\bar{2}0]$ or [110] zone axis, and (g) reference structural orientation.

4. Discussion

Though the elastic scattering cross section is small for both high-energy ion irradiations, Fig. 1d to 1i clearly demonstrates that collision cascades [46] will stochastically occur for each ion. It was demonstrated earlier that elastic collisions from a higher S_n contribution are

necessary to form the FCC-MAX phase, but there is a clear distinction in the FCC profile intensity between 4 *MeV* Au and 17 *MeV* Pt while the damage dose (~3 dpa) is similar. It has been demonstrated recently in the literature that low-energy Au ions require a fluence roughly 2 orders of magnitude greater than that employed here ($\sim 1\times10^{16}$ cm^{-2}) to produce FCC-MAX profiles with relative intensity similar to those observed following the high-energy Pt irradiation [38]. Recall that formation of the FCC-MAX involves a site shift to the β-Ti_3SiC_2 position, so the added energy deposition from the 17 *MeV* Pt ion thermal spike could effectively reduce this barrier to forming the FCC-MAX. This is consistent with the depth profile analysis from the previous study, which demonstrated that with other contributions being equal, increasing S_e above the 4 $keV\ nm^{-1}$ threshold leads to an increase in FCC-type relative intensity [31]. This sort of S_e threshold for enhanced phase transformation to a higher symmetry phase has been observed in other material systems in the past, most notably in zirconia. Pure, unstabilized zirconia has a monoclinic structure that, following high fluence irradiations at low temperatures with 340 *keV* Xe ions, partially transforms to a higher symmetry tetragonal phase [59]. However, when irradiating at room temperature with ions where S_e exceeds a 12 $keV\ nm^{-1}$ threshold, the percent phase transformed increases significantly, in fact, linearly with S_e, and the fluence to reach the saturated transformation is reduced by over two orders of magnitude [60]. Therefore, the enhanced transformation from α-Ti_3SiC_2 to FCC-MAX with added {111} twin symmetry by S_e exceeding a 4 $keV\ nm^{-1}$ threshold is not unprecedented.

It also appears the relationship between the thermal spike radii and the radial distribution of collision events is vital to this phase formation as the 14 *MeV* Cl irradiations do not show a clear, if any, increase in a FCC-MAX profile; though, there is an equivalent S_e deposition from the 17 *MeV* Pt irradiations. This suggests that while a S_e greater than the 4 $keV\ nm^{-1}$ threshold will exacerbate the formation of FCC-MAX by elastic collisions, increasing the

S_e/S_n will eventually suppress the effect. This is corroborated in the reduced FCC-MAX to MAX phase profile intensity at a similar S_e and damage dose following 9 *MeV* Ti ion irradiation, see the reduction in the relative intensity heat map in Fig. 2, as the S_e/S_n of this condition lies between that of the high-energy irradiations of this study. This is not to say that Ti-Si anti-site and C Frenkel pair production due to the stochastic elastic collisions and inelastic thermal spike shock waves are not occurring, but rather the formation of FCC-MAX is suppressed by annealing as the thermal spike exceeds the radii of collision events. That said, this annealing does not appear to be sufficient to "heal" pre-existing FCC-MAX, as the broad peaks in both the diffraction and Raman profiles for Au ion pre-damaged material irradiated with the high-energy Cl ions appear mainly unchanged.

The above effects may be observed indirectly through the significant increase in the $\Delta c/c_0$ and $\Delta a/a_0$ with increasing S_e/S_n when the FCC phase content does not increase. It has been previously observed that the inclusion of FCC TiC reduced irradiation swelling and other anisotropic lattice distortion in microstructures [61]. It is expected that the formation of a FCC phase, whether TiC_x or a FCC-MAX, embedded in the hexagonal MAX structure, would perform similarly by accommodating the point defects in the structural transformation, reducing the lattice strain. This is seen in the highly reduced lattice strain in the cases of low-energy Au and Xe and high-energy Pt irradiations, all of which show signatures from the FCC and β-Ti_3SiC_2 structure in GIXRD profiles and SAED patterns [39]. Conversely, if FCC-MAX phase formation is suppressed, the point defects and Ti-Si anti-sites will lead to increased distortion of the c/a [30,32,33,35], as is seen comparing between Fig. 2 and 4. Moreover, in the case of high-energy Cl irradiation, where the formation of additional FCC-phase appears fully suppressed, both in GIXRD and SAED patterns, the lattice strain appears to have reached a local maximum. Looking beyond the S_e/S_n regimes of this study, the literature results included in Fig. 4 also do not show any broad FCC-type peak profiles in

GIXRD. However, they also continue the Fig. 4 trend with c and a-LP maximum strain levels around 1.3% and -0.3%, respectively, [23,56] values that match those calculated for a high Ti-Si anti-site concentration in an otherwise pristine Ti_3SiC_2 lattice [30]. It should be noted that following swift heavy ion (SHI) irradiation, changes in diffraction profiles have not been observed [23]. Following the proposed suppression of the FCC-MAX formation by the thermal spike, this makes sense, as S_e/S_n will be significantly higher for the ion; however, there is also a lack of lattice strain. It is possible, with such a low S_n and damage dose (dpa) orders of magnitude lower than those reached in this study, that the production of defects is insufficient to result in a measurable strain, suggesting a minimum S_n or dose to damage by this mechanism. Alternatively, in the SHI regime, the thermal spike may achieve a significantly higher temperature, leading to localized melting and relaxation of any resulting lattice strain, suggesting a maximum S_e, above which strain is not observed. However, the energy regimes of this study are not attuned to answer this question, and further postulation would be speculative. For now, what may be suggested is a second threshold of the ratio of $S_e/S_n > 150$ to suppress FCC-MAX phase formation and maximize relative c/a distortion when ion energy is $< 1\ MeV\ amu^{-1}$.

It may also be observed that while additional FCC-MAX phase formation is suppressed by the high S_e/S_n, the contribution of pre-existing defects serves to significantly increase the maximum for the lattice strain at these fluences. This increase is well beyond that of an additive contribution and represents a synergy between the inelastic energy dissipation and evolving defect concentration, whereby the thermal spike is more radially confined by defects inhibiting the dissipation of energy to and through the lattice and thus increasing the local temperature differential and subsequent shock wave [9,10,40-42,57]. This radial confinement may be sufficient to prevent complete annealing of the pre-damaged FCC-MAX phase by high-energy Cl ions but not to suppress increased formation of the phase.

The implications of these results for the selection of ion species and energy regimes for irradiation studies in MAX phases cannot be overstated. Typically, higher energy (10-50 *MeV*) medium mass self-ions and light ions are recommended to extend the "safe" analysis depth range and avoid artifacts due to surface effects and ion concentration profiles [6]. However, for this composition, two additional constraints are now recognized as vital to the selection of ions. Exceeding a low, 4 $keV\ nm^{-1}$ threshold in S_e dramatically increases the ballistically driven FCC-MAX formation, resulting from the elastic collision cascades. At the same time, radial confinement of the ballistic processes, when S_e/S_n is large, suppresses this phase formation and enhances measured lattice strain. Additionally, as energy loss pathways will change with depth for ion irradiation, an appropriate depth probe must be selected for subsequent characterization, such that the S_e/S_n is consistent. In the case of direct comparison with different reactor environments, the 14 *MeV* Cl ions have a comparable S_e/S_n to a mixed spectrum LWR while the 17 *MeV* Pt ions may be compared with a fast fission reactor environment [11]. Direct comparison of the results of this study and these reactor environments is limited as operational temperatures significantly exceed the room temperature *in situ* conditions. That said, elevated temperature *in situ* ion and neutron irradiation conditions have been previously observed to only partially mitigate these observed effects [29,33,34], so the direct influence of the energy loss pathways observed here are proposed to remain consistent in reactor. It is also important to recognized that using ions to take advantage of the significant difference in dose rates may inherently influence the defect accumulation rates at sinks or other defect clusters [6]. That said, estimating the highest flux seen in this study ($\sim 10^{12}\ cm^{-2}s^{-1}$) equates to approximately $\sim 10^{-14}\ nm^{-2}ps^{-1}$. Then, even assuming an extreme case of a thermal spike event lasting 10 *ms* (10^{10} *ps*), when they are typically <<100 *ps* in thermally similar materials such as SiC, there is a $<10^{-2}$ probability of two thermal spikes occupying the same 100 nm^2 area. Therefore, it is reasonable to consider

that even at these higher dose rates, there will not be an impact on the energy loss effects, and the ion events may be treated as uncoupled in both space and time [31,35,57]. With all these considerations, care should be taken when selecting ions as a tool for direct comparison to bulk elastic collision environments, such as those under neutron irradiation, and high-energy self-ions may not be the appropriate tool for making such comparisons in Ti_3SiC_2.

5. Conclusions

In summary, the effects of electronic and nuclear energy dissipation during ion irradiation of Ti_3SiC_2 have been found to be competing and synergistic for different ratios of electronic to nuclear energy loss. Nuclear energy loss results in elastic collision cascades, leading to the formation of a FCC-MAX phase with Ti-Si anti-site defects. This FCC phase serves to partially relax the structure and resist the overall anisotropic c/a distortion. Intense electronic energy loss above a S_e threshold of 4 $keV\ nm^{-1}$ serves to exacerbate this effect through the thermal spike adding energy to the lattice and increasing point defects through shock waves. However, increasing the ratio of S_e/S_n serves to add sufficient energy over the radial distribution of collision events that formation of the FCC-MAX phase is suppressed, thus maximizing lattice strain for energy regimes < 1 $MeV\ amu^{-1}$. There is a threshold for this ratio of $S_e/S_n > 150$, where the FCC-MAX phase formation is fully suppressed and lattice strain is maximized. Further, there is a synergy between pre-existing defects and electronic energy loss, whereby the effects of the thermal spike are more radially confined, thus significantly increasing the resultant strain. These results further illustrate that the interaction of both electronic and nuclear energy dissipation pathways is vital to the study of irradiation effects of materials such as Ti_3SiC_2.

6. Acknowledgments

This research was supported by the University of Tennessee Office of the Chancellor, the University of Tennessee Governor's Chair program, and the State of Tennessee and Tennessee Higher Education Commission (THEC) through their support of the Center for

Materials Processing. The authors would like to thank Dr. Michael Koehler for his assistance within the Joint Institute for Advanced Materials (JIAM) diffraction facility, and both Dr. Gerd Duscher and Dr. John Dunlap for their assistance in the JIAM microscopy facility. Finally, the authors would like to thank Chris Ostrouchov for his invaluable assistance with Python 3.6 programming to implement the iterative c/a method as well as collision analysis through pysrim.

7. References

[1] G.H. Kinchin, R.S. Pease, The Displacement of Atoms in Solids by Radiation, Rep. Prog. Phys. 18 (1) (1955), 1–51. doi:10.1088/0034-4885/18/1/30.

[2] J. Lindhard, M. Scharff, Energy Dissipation of Ions in the kev Region, Phys. Rev. 124 (1) (1961) 128–130.

[3] J.C. Bourgoin, J.W. Corbett, Ionization enhanced diffusion, J. Chem. Phys. 59 (6) (1973) 4042–4046. doi:10.1063/1.433143

[4] G.B. Krefft, Ionization-stimulated annealing effects on displacement damage in magnesium oxide, J. Vac. Sci. Tech. 14 (1) (1977) 533–536. doi:10.1116/1.569301.

[5] W.K. Chu, Energy Loss of Charged Particles, in: J.P. Thomas, A. Cachard (Eds.), Material Characterization Using Ion Beams, Springer US, Boston, MA, 1978, pp. 3–34. doi:10.1007/978-1-4684-0856-0 1.

[6] S.J. Zinkle, L.L. Snead, Scripta Mater. Opportunities and limitations for ion beams in radiation effects studies : Bridging critical gaps between charged particle and neutron irradiations, Scripta Mater. 143 (2018) 154–160. doi:10.1016/j.scriptamat.2017.06.041.

[7] S.J. Zinkle, Effect of irradiation spectrum on the microstructural evolution in ceramic insulators, J. Nucl. Mater. 219 (1995) 113-127. doi:10.1016/0022-3115(94)00662-8.

[8] N. Sellami, A. Debelle, M.W. Ullah, H.M. Christen, J.K. Keum, H. Bei, H. Xue, W.J. Weber, Y. Zhang, Effect of electronic energy dissipation on strain relaxation in irradiated

concentrated solid solution alloys, Curr. Opin. Solid St. Mater. Sci. In Press, Corrected Proof (6 March 2019) doi:10.1016/j.cossms.2019.02.002

[9] P. Liu, Y. Zhang, H. Xue, K. Jin, M.L. Crespillo, X. Wang, W.J. Weber, A coupled effect of nuclear and electronic energy loss on ion irradiation damage in lithium niobate, Acta Mater. 105 (2016) 429–437. doi:10.1016/j.actamat.2015.12.048.

[10] H. Xue, Y. Zhang, W.J. Weber, In-cascade ionization effects on defect production in 3C silicon carbide, Mater. Res. Lett. 5 (7) (2017) 494–500. doi:10.1080/21663831.2017.1334241.

[11] S.J. Zinkle, L.R. Greenwood, Summary of ionizing and displacive irradiation fields in various facilities, Fus. React. Mater. Semiannu. Prog. Rep. DOE/ER-0313/14 (1993) 74–78.

[12] V.H. Nowotny, Strukturchemie einiger Verbindungen der Ubergangsmetalle mit den elementen C, Si, Ge, Sn, Prog. Solid St. Chem. 5 (C) (1971) 27–70. doi:10.1016/0079-6786(71)90016-1.

[13] V.H. Nowotny, P. Rogl, J.C. Schuster, Structural chemistry of complex carbides and related compounds, J. Solid St. Chem. 44 (1) (1982) 126–133. doi:10.1016/0022-4596(82)90409-1.

[14] M.W. Barsoum, T. El-Raghy, Synthesis and characterization of a remarkable ceramic: Ti3SiC2, J. Am. Ceram. Soc. 79 (7) (1996) 1953–1956. doi:10.1111/j.1151-2916.1996.tb08018.x.

[15] M.W. Barsoum, The Mn+1AXn Phases: A new Class of Solids; Thermodynamically Stable Nanolaminates, Prog. Solid St. Chem. 28 (2000) 201–281.

[16] T.H. Scabarozi, S. Amini, O. Leaffer, A. Ganguly, S. Gupta, W. Tambussi, S. Clipper, J.E. Spanier, M.W. Barsoum, J.D. Hettinger, S.E. Lofland, Thermal expansion of select Mn+1AXn(M=early transition metal, A=A group element, X=C or N) phases measured

by high temperature x-ray diffraction and dilatometry, J. App. Phys. 105 (1) (2009) 1–8. doi:10.1063/1.3021465.

[17] M.W. Barsoum, MAX Phases: Properties of Machinable Ternary Carbides and Nitrides, Wiley-VCH, Weinheim, Germany, 2013.

[18] M. Radovic, M. Barsoum, T. El-Raghy, S. Wiederhorn, W. Luecke, Effect of temperature, strain rate and grain size on the mechanical response of Ti3SiC2 in tension, Acta Mater. 50 (6) (2002) 1297–1306. doi:10.1016/S1359-6454(01)00424-4.

[19] E. Hoffman, D. Vinson, R. Sindelar, D. Tallman, G. Kohse, M. Barsoum, MAX phase carbides and nitrides: Properties for future nuclear power plant in-core applications and neutron transmutation analysis, Nucl. Eng. Des. 244 (2012) 17–24. doi:10.1016/j.nucengdes.2011.12.009.

[20] S.J. Zinkle, Advanced irradiation-resistant materials for Generation IV nuclear reactors, in: P. Yvon (Ed.), Woodhead Publishing Series in Energy Number 106: Structural Materials for Generation IV Nuclear Reactors, Woodhead Publishing, Elsevier Ltd., Cambridge, MA, 2017, Ch. 16, pp. 569–594.

[21] J.C. Nappé, P. Grosseau, F. Audubert, B. Guilhot, M. Beauvy, M. Benabdesselam, I. Monnet, Damages induced by heavy ions in titanium´ silicon carbide: Effects of nuclear and electronic interactions at room temperature, J. Nucl. Mater. 385 (2) (2009) 304–307. doi:10.1016/j.jnucmat.2008.12.018.

[22] K. Whittle, M. Blackford, R. Aughterson, S. Moricca, G. Lumpkin, D. Riley, N. Zaluzec, Radiation tolerance of Mn+1AXn phases, Ti3AlC2 and Ti3SiC2, Acta Mater. 58 (13) (2010) 4362–4368. doi:10.1016/j.actamat.2010.04.029.

[23] J.C. Nappé, I. Monnet, P. Grosseau, F. Audubert, B. Guilhot, M. Beauvy, M. Benabdesselam, L. Thomé, Structural changes induced by heavy ion irradiation in

titanium silicon carbide, J. Nucl. Mater. 409 (1) (2011) 53–61. doi:10.1016/j.jnucmat.2010.12.235.

[24] C. Liu, L. Shi, Q. Qi, D.J. O'Connor, B.V. King, E.H. Kisi, X.B. Qing, B.Y. Wang, Surface damage of Ti3SiC2 by MeV iodine bombardment, Nucl. Instrum. Methods Phys. Res. Sect. B Beam Interact. Mater. Atoms 307 (2013) 536–540. doi:10.1016/j.nimb.2013.03.021.

[25] Q. Qi, G. Cheng, L. Shi, D. O'Connor, B. King, E. Kisi, Damage accumulation and recovery in C+-irradiated Ti3SiC2, Acta Mater. 66 (2014) 317–325. doi:10.1016/j.actamat.2013.11.019.

[26] M.K. Patel, D.J. Tallman, J.A. Valdez, J. Aguiar, O. Anderoglu, M. Tang, J. Griggs, E. Fu, Y. Wang, M.W. Barsoum, Effect of helium irradiation on Ti3AlC2 at 500C, Scripta Mater. 77 (2014) 1–4. doi:10.1016/j.scriptamat.2013.12.010.

[27] D.J. Tallman, E.N. Hoffman, E.N. Caspi, B.L. Garcia-Diaz, G. Kohse, R.L. Sindelar, M.W. Barsoum, Effect of neutron irradiation on select MAX phases, Acta Mater. 85 (2015) 132–143. doi:10.1016/j.actamat.2014.10.068.

[28] W. Jiang, C.H. Henager, T. Varga, H.J. Jung, N.R. Overman, C. Zhang, J. Gou, Diffusion of Ag, Au and Cs implants in MAX phase Ti3SiC2, J. Nucl. Mater. 462 (2015) 310–320. doi:10.1016/j.jnucmat.2015.04.002.

[29] D. Clark, S. Zinkle, M. Patel, C. Parish, High temperature ion irradiation effects in MAX phase ceramics, Acta Mater. 105 (2016) 130–146. doi:10.1016/j.actamat.2015.11.055.

[30] J. Ward, S. Middleburgh, P. Frankel, M. Topping, A. Garner, D. Stewart, M.W. Barsoum, M. Preuss, Crystallographic evolution of MAX phases in proton irradiating environments, J. Nucl. Mater. 502 (2018) 220–227. doi:10.1016/j.jnucmat.2018.02.008.

[31] W.A. Hanson, M.K. Patel, M.L. Crespillo, Y. Zhang, W.J. Weber, Influence of electronic vs nuclear energy loss in radiation damage of Ti3SiC2, Acta Mater. 161 (2018) 302–310. doi:10.1016/j.actamat.2018.09.027.

[32] H. Zhang, J. Wang, J. Wang, Y. Zhou, S. Peng, X. Long, Role of Nanolaminated Crystal Structure on the Radiation Damage Tolerance of Ti3SiC2 : Theoretical Investigation of Native Point Defects, J. Nanomater. 2013 (2013) 1–5. doi:10.1155/2013/831590.

[33] D.J. Tallman, L. He, B.L. Garcia-Diaz, E.N. Hoffman, G. Kohse, R.L. Sindelar, M.W. Barsoum, Effect of neutron irradiation on defect evolution in Ti3SiC2 and Ti2AlC, J. Nucl. Mater. 468 (2016) 194–206. doi:10.1016/j.jnucmat.2015.10.030.

[34] D.J. Tallman, L. He, J. Gan, E.N. Caspi, E.N. Hoffman, M.W. Barsoum, Effects of neutron irradiation of Ti3SiC2 and Ti3AlC2 in the 121 − 1085C temperature range, J. Nucl. Mater. 484 (2016) 120–134. doi:10.1016/j.jnucmat.2016.11.016.

[35] W.A. Hanson, The response of Ti_3SiC_2 MAX phase to ion energy dissipation during energetic irradiations at different temperatures, The University of Tennessee, Knoxville, 2019.

[36] L. Zhang, Q. Qi, L. Shi, D. O'Connor, B. King, E. Kisi, D. Venkatachalam, Damage tolerance of Ti3SiC2 to high energy iodine irradiation, App. Surf. Sci. 258 (17) (2012) 6281–6287. doi:10.1016/j.apsusc.2012.03.022.

[37] T. Yang, C. Wang, W. Liu, S. Liu, J. Xiao, Q. Huang, J. Xue, S. Yan, Y. Wang, Formation of nano-twinned structure in Ti3AlC2 induced by ion-irradiation, Acta Mater. 128 (2017) 1–11. doi:10.1016/j.actamat.2017.01.066.

[38] C. Wang, T. Yang, C.L. Tracy, C. Lu, H. Zhang, Y.J. Hu, L. Wang, L. Qi, L. Gu, Q. Huang, J. Zhang, J. Wang, J. Xue, R.C. Ewing, Y. Wang, Disorder in Mn+1AXn phases at the atomic scale, Nat. Commun. 10 (622) (2019) 1–9. doi: 10.1038/s41467-019-08588-1.

[39] Q. Huang, R. Liu, G. Lei, H. Huang, J. Li, S. He, D. Li, L. Yan, J. Zhou, Irradiation resistance of MAX phases Ti3SiC2 and Ti3AlC2: Characterization and comparison, J. Nucl. Mater. 465 (2015) 640–647. doi:10.1016/j.jnucmat.2015.06.056.

[40] L. Thomé, G. Velisa, S. Miro, A. Debelle, F. Garrido, G. Sattonnay, S. Mylonas, P. Trocellier, Y. Serruys, Recovery effects due to the interaction between nuclear and electronic energy losses in SiC irradiated with a dual-ion beam, J. App. Phys. 117 (10) (2015) 1–9. doi:10.1063/1.4914305.

[41] E. Zarkadoula, M. Toulemonde, W. J. Weber, Additive effects of electronic and nuclear energy losses in irradiation-induced amorphization of zircon, App. Phys. Lett. 107 (26) (2015). doi:10.1063/1.4939110.

[42] H. Xue, E. Zarkadoula, R. Sachan, Y. Zhang, C. Trautmann, W.J. Weber, Synergistically-enhanced ion track formation in pre-damaged strontium titanate by energetic heavy ions, Acta Mater. 150 (2018) 351–359. doi:10.1016/j.actamat.2018.03.027.

[43] P. Eklund, M. Beckers, U. Jansson, H. Hogberg, L. Hultman, The Mn+1AXn phases: Materials science and thin-film processing, Thin Solid Films 518 (8) (2010) 1851–1878. doi:10.1016/j.tsf.2009.07.184.

[44] J.F. Ziegler, M. Ziegler, J.P. Biersack, SRIM The stopping and range of ions in matter (2010), Nucl. Instrum. Methods Phys. Res. Sect. B Beam Interact. Mater. Atoms 268 (11-12) (2010) 1818–1823. doi:10.1016/j.nimb.2010.02.091.

[45] J.F. Ziegler, J.P. Biersack, M.D. Ziegler, SRIM 2013, Software code. SRIM - The Stopping and Range of Ions in Matter (2013).

[46] C. Ostrouchov, Y. Zhang, W.J. Weber, pysrim: Automation, Analysis, and Plotting of SRIM Calculations, J. Open Sour. Softw. 3 (2018) 10-12. doi:10.21105/joss.00829.

[47] B. Liu, B. Petersen, Y. Zhang, J. Wang, W.J. Weber, Layered Structure Induced Anisotropic Low-Energy Recoils in Ti3SiC2, J. Am. Ceram. Soc. 99 (8) (2016) 2693–2698. doi:10.1111/jace.14277.

[48] Y. Zhang, M.L. Crespillo, H. Xue, K. Jin, C.H. Chen, C.L. Fontana, J.T. Graham, W.J. Weber, New ion beam materials laboratory for materials modification and irradiation effects research, Nucl. Instrum. Methods Phys. Res. Section B Beam Interact. Mater. Atoms 338 (2014) 19–30. doi:10.1016/j.nimb.2014.07.028.

[49] M. Crespillo, J. Graham, Y. Zhang, W.J. Weber, Temperature measurements during high flux ion beam irradiations, Rev. Sci. Instrum. 87 (2) (2016) 1–7. doi:10.1063/1.4941720.

[50] B. Henke, E. Gullikson, J. Davis, X-ray interactions: photoabsorption, scattering, transmission, and reflection at e=50-30000 ev, z=1-92, Atomic Data and Nuclear Data Tables 54 (no.2) (1993) 181–342.

[51] OriginPro (OriginLab, Northampton, MA).

[52] M. Marciszko, Diffraction study of mechanical properties and residual stresses resulting from surface processing of polycrystalline materials, AGH - University of Science and Technology, 2013.

[53] J. Xiao, T. Yang, C. Wang, J. Xue, Y. Wang, Investigations on radiation tolerance of Mn+1AXn phases: Study of Ti3SiC2, Ti3AlC2, Cr2AlC, Cr2GeC, Ti2AlC, and Ti2AlN, J. of the American Ceramic Society 98 (4) (2015) 1323–1331. doi:10.1111/jace.13450.

[54] M. Amer, M.W. Barsoum, The Raman spectrum of Ti3SiC2., J. App. Phys. 84 (10) (1998) 5817.

[55] U.D. Wdowik, A. Twardowska, M. Mędala-Wąsik, Lattice dynamics of binary and ternary phases in Ti-Si-C system: A combined Raman spectroscopy and density functional theory study, Mater. Chem. Phys. 168 (2015) 58–65. doi:10.1016/j.matchemphys.2015.10.057.

[56] J.C. Nappé, I. Monnet, F. Audubert, P. Grosseau, M. Beauvy, M, Benabdesselam, Formation of nanosized hills on Ti3SiC2 oxide layer irradiated with swift heavy ions. Nucl. Instrum. Methods Phys. Res. Section B Beam Interact. Mater. Atoms, 270 (2012) 36–43. doi:10.1016/j.nimb.2011.09.027

[57] Y. Zhang, H. Xue, E. Zarkadoula, R. Sachan, C. Ostrouchov, P. Liu, X.L. Wang, S. Zhang, T.S. Wang, W.J. Weber, Coupled electronic and atomic effects on defect evolution in silicon carbide under ion irradiation. Curr. Opin. Solid St. Mater. Sci. 21(6) (2017) 285–298. doi:10.1016/j.cossms.2017.09.003

[58] E. Zarkadoula, K. Jin, Y. Zhang, W.J. Weber, Synergistic effects of nuclear and electronic energy loss in KTaO<inf>3</inf>under ion irradiation, AIP Adv. 7 (1) (2017) 1–7. doi:10.1063/1.4973938.

[59] K.E. Sickafus, H. Matzke, T. Hartmann, K. Yasuda, J.A. Valdez, P. Chodak, R.A. Verrall, Radiation damage effects in zirconia. J. Nucl. Mater., 274 (1999) 66–77. doi:10.1016/S0022-3115(99)00041-0

[60] A. Benyagoub, Complete phase transformation in zirconia induced by very high electronic excitations. Nucl. Instrum. Methods Phys. Res. Section B Beam Interact. Mater. Atoms, 268 (19) (2010) 2968–2971. doi:10.1016/j.nimb.2010.05.019

[61] S.J. Zinkle, G.S. Was, Materials challenges in nuclear energy, Acta Mater. 61 (3) (2013) 735–758. doi:10.1016/j.actamat.2012.11.004.